Dynamic modelling of trickle bed reactor

Hachhach, Mouad; Russo, Vincenzo; Murzin, Dmitry Yu; Salmi, Tapio

Published in:
Powder Technology

DOI:
10.1016/j.powtec.2023.118608

Published: 01/07/2023

Document Version
Final published version

Document License
CC BY

Powder Technology 425 (2023) 118608

Contents lists available at ScienceDirect

Powder Technology

journal homepage: www.journals.elsevier.com/powder-technology

Dynamic modelling of trickle bed reactor: Case study of arabinose oxidation

Mouad Hachhach [a], Vincenzo Russo [a,b], Dmitry Yu. Murzin [a], Tapio Salmi [a,*]

[a] Åbo Akademi University, Laboratory of Industrial Chemistry and Reaction Engineering (TKR), Åbo-Turku FI-20500, Finland
[b] Università di Napoli Federico II, Chemical Sciences, Complesso Universitario Monte S. Angelo, Napoli IT-80126, Italy

HIGHLIGHTS

- Development of 3 phases dynamic trickle bed reactor model.
- Developed model was used to study the arabinose oxidation.
- Effect of shape and size of catalyst was studied numerically.
- Model was successfully implemented in gProms.

GRAPHICAL ABSTRACT

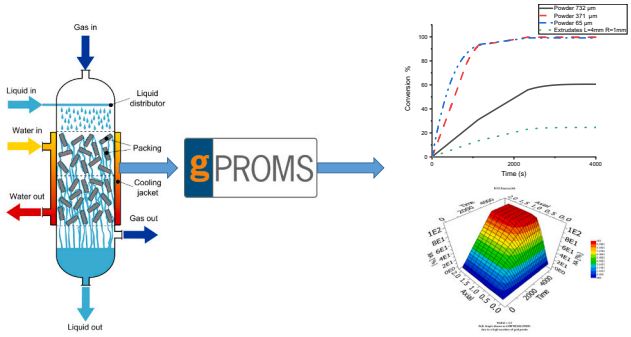

ARTICLE INFO

Keywords:
gProms
Trickle bed reactors
Arabinose oxidation
Kinetics
Transport phenomena

ABSTRACT

Trickle beds are among the most used reactors in different sectors of chemical industries. In this work the aim was to develop a general heterogeneous multiscale model for continuous trickle bed reactors, which enables the calculation of instantaneous concentration and temperature changes as well as the stationary behaviour of the reactor. The model development was based on solving simultaneously both the energy and mass balances for the continuous gas and liquid phases and for the stagnant catalyst particles. Mass transfer coefficients and pressure drop equations from well-established correlations were used. The developed model is aimed to be as general as possible in order to be used as a framework for other kind of bed reactors and arbitrary reaction schemes.

The model can be simplified taking into consideration only one or two phases, and in this case it was applied to catalytic sugar oxidation to sugar acid and the effect of catalyst shape and size was investigated. Simulation results revealed that complete sugar conversion was achieved only for small catalyst particles, also the length of the reactor affects the conversion of arabinose more than the residence time or the bed radius: in fact for much bigger particles the conversion can also be achieved for longer reactor beds.

1. Introduction

Currently, our society is facing many socio-economic and environmental challenges that are directly or implicitly linked to our strong dependence on fossil feedstock which is the main cause of global warming with all its harmful effects. Thererfore it is necessary to shift to more clean and renewable feedstock which is biomass. As an analogy to classical refineries, biorefineries are industrial facilities that convert almost all kinds of biomass into valuable products such as biofuels and

* Corresponding author.
E-mail address: tapio.salmi@abo.fi (T. Salmi).

https://doi.org/10.1016/j.powtec.2023.118608
Received 20 August 2022; Received in revised form 21 April 2023; Accepted 28 April 2023
Available online 29 April 2023

Nomenclature

α	Exponent in catalyst activity function
η_{H2O}	Viscosity of water
ΔH_r	Reaction enthalpy
λ_p	Particle heat conductivity
$\lambda_{r,\ L}$	Radial heat conductivity of liquid phase
$\lambda_{r,\ G}$	Radial heat conductivity of gas phase
$\lambda_{z,\ L}$	Axial heat conductivity of liquid phase
$\lambda_{z,\ G}$	Axial heat conductivity of gas phase
ρ_{cat}	Catalyst density
ρ_L	Density of liquid phase
σ_{H2O}	Surface tension of water
A	Arrhenius constant, pre-exponential factor
a^*	Limiting activity factor
a_{sp}	Catalyst surface area-to-volume, $a_{sp} = \frac{3}{R_p}$
$C_{i,j}$	Concentration of compound i in phase j
$CO_{2,\ S}$	Saturation concentration of oxygen
$c_{p,\ cat}$	Specific heat of catalyst
$c_{p,\ L}$	Specific heat of liquid phase
$c_{p,\ G}$	Specific heat of gas phase
$D_{eff,i}$	Effective diffusivity of compound i
d_K	Krisher-Kast hydraulic diameter, $d_K = 2R_p\sqrt[2]{\frac{16\varepsilon_p{}^3}{9\pi(1-\varepsilon_p{}^2)}}$
DL	Diffusivity of arabinose in aqueous solution
h_w	Wall heat transfer coefficient
$h_G a$	Gas–liquid heat transfer coefficient
k	Rate constant
L	Reactor length
m(O2)	Molar mass of oxygen
R	Reactor radius
Rp	Particle radius
Pe_L	Peclet number of liquid phase
Pe_G	Peclet number of gas phase
T_j	Temperature of phase j

chemicals [1]. Lignocellulosic biomass is of particular interest in the context of renewables, being the most abundant natural biomass globally with an approximate yield of about 200 billion tons [2] and being able to meet the requirements for both energy generation and production of high value-added products. The use of lignocellulosic biomass avoids the very controversial competition with agricultural commodities since this feedstock is non-edible [3,4]. Lignocellulosic biomass consists of cellulose, lignin and hemicelluloses, the latter ones are known as the second most abundant carbohydrate material contributing to 25–35% of the dry weight of wood [5]. Typical hemicelluloses appearing in lignocellulosic biomass are glucomannan, galactoglucomannan, arabinogalactan and glucuronoxylan. Arabinogalactan is a hemicellulose composing up to 15% of the softwood of larch species *(Larix sibirica)* [6]. Controlled hydrolysis of arabinogalactan under mild conditions allows the obtention of the monomeric sugars galactose and arabinose which can be later converted to sugar acids using selective catalytic oxidation using a slurry reactor or a trickle bed reactor. The sugar acids are considered to be a high-value products due to their various applications, such as sequestering agents and binders, corrosion inhibitors, biodegradable chelators for pharmaceuticals and pH regulators. They are also used in the production of high-added value production synthetic polymers, such as polyamides, polyesters, and hydrogels [7]. The market size for glucaric acid, for example, is worth 1.30 billion USD by 2025 with a Compound annual growth rate (CAGR) of 10.1% [8] .

Trickle bed reactors can be defined as continuous three-phase bed reactors containing a packed bed of catalyst particles, where the liquid flows downwards [9]. Trickle beds offer several advantages because such as simplicity in operation, flexibility for a variety of materials, high catalyst loading per unit volume, and low capital and operating costs as well as relatively low energy consumption, higher gas conversion rates and productivities compared to tank and bubble column reactors [10–12]. Thanks to these properties trickle beds are used in diverse fields of chemical industries such petroleum, petrochemical, fine chemicals and biochemical industries [13,14].

The history of these kind of reactors can be traced back to the 18th century with early applications mainly in waste water treatment. Later on these reactors become quite popular in industrial production due to their previously mentioned unique properties and high production capacity: in fact the worldwide annual capacity of materials processed via trickle bed reactors is around 1.6 billion metric tons [11] which correspond to a value of the order of $300 Billion/year in 1998 [15]. These numbers and the interest in trickle bed reactors are steadily increasing, which encourages to the development of the reactor technology in industrial plants. To achieve this objective, advanced mathematical modelling is required [16].

Modelling and simulation tools are nowadays frequently used for process design, optimization and scale-up [17], because they provide a reliable, inexpensive and rapid way to investigate the impact of design parameters on the overall process performance [18]. Most of the research dealing with trickle bed reactor modelling has been focused on small-scale reactors [19–22] or industrial scale ones in petrochemical applications [18,23,24]. In this work, we applied a generic approach to develop a comprehensive trickle bed reactor model, which was based on mass and energy balances and classical correlations for pressure drop and transport phenomena. The heterogeneous character of the model, i. e. the interaction of the gas and liquid phases with solid catalyst particles was in the focus of the work. A program code in gProms was written to solve the mass and energy balance equations numerically in a very efficient way. The obtained results can be used as framework for the modelling of various reaction systems as well as powerful tool to assist process design, scale-up and life cycle assessment for all possible reactions where trickle bed is an option.

2. General model of the trickle bed reactor

2.1. Model development

The objective of this work was to develop a general model for multiscale three-phase catalytic trickle bed reactors enabling the computation the concentration and temperature fields at various locations and reaction rates. The local and instantaneous concentration and temperature profiles were simulated by solving simultaneously the energy and mass balances of the different species inside the reactor tube. Because of the general characteristics, the model can be simplified by taking into consideration one or two phases only. The model was applied to the process of sugar oxidation to sugar acids. The model can be used for scale-up, too.

2.1.1. Mass balances

The concentration and temperature profiles inside the reactor (axial and radial locations) and in the catalyst particles were calculated by solving the mass and energy balances simultaneously together with semi-empirical correlations for pressure drop, fluid dynamics and kinetic laws. It was presumed that all the reactions occur inside the catalyst particles and thus the reaction rate term appears only in the mass balance of the solid. The active catalyst species is assumed to be

distributed evenly inside the catalyst particle. Similarly to previous articles published by our group [19,21] the mass balances of gas phase shown in Eq. (1) affirms that the accumulation term is the sum of gas-liquid mass as well as axial and radial dispersion alongside the convection terms. The state variables of the mass balances are the gas phase concentrations of each component i $C_{i,\ G}(t,z,r)$ at the radial and axial locations r and z, respectively and at the time moment t. The remaining parameters (gas liquid mass transfer coefficient, dispersion coefficient, holdup) were calculated via well-established correlations from the literature as will be elaborated later.

$$\varepsilon_G \frac{\partial C_{i,G}(t,z,r)}{\partial t} = -k_{i,L}a\left(C^{*}_{i,L}(t,z,r) - C_{i,L}(t,z,r)\right) - \frac{\partial\left(u_G(z,r)C_{i,G}(t,z,r)\right)}{\partial z} + \varepsilon_G\, D_{z,G}(z,r)\frac{\partial^2 C_{i,G}(t,z,r)}{\partial z^2} + \varepsilon_G\, D_{r,G}(z,r)\left(\frac{\partial^2 C_{i,G}(t,z,r)}{\partial r^2} + \frac{1}{r}\,\frac{\partial C_{i,G}(t,z,r)}{\partial r}\right) \tag{1}$$

The liquid-phase mass balance is shown in Eq. (2), in which the accumulation term is the net sum of gas-liquid mass transfer coefficient, in addition to the convection and axial and radial dispersion terms, and finally the mass transfer flux from/to the solid phase as the shown in the last term. The latter one is the solid-phase concentration of component i on the catalyst surface at the instant t and at the axial location z. Similarly to the gas phase mass balance, the state variables are the liquid phase concentrations $C_{i,\ L}(t,z,r)$ at the time t and at the axial and radial locations z and r, respectively. The key parameters needed to calculate the concentrations in the liquid phase are the holdup, liquid velocities, axial and radial dispersion coefficients, catalyst shape factor and effective diffusivity.

$$\varepsilon_L \frac{\partial C_{i,L}(t,z,r)}{\partial t} = k_{i,L}a\left(C^{*}_{i,L}(t,z,r) - C_{i,L}(t,z,r)\right) - u_L\,\frac{\partial\left(C_{i,L}(t,z,r)\right)}{\partial z} + \varepsilon_L D_{z,L}\frac{\partial^2 C_{i,L}(t,z,r)}{\partial z^2} + \varepsilon_L D_{r,L}\left(\frac{\partial^2 C_{i,L}(t,z,r)}{\partial r^2} + \frac{1}{r}\,\frac{\partial C_{i,L}(t,z,r)}{\partial r}\right) - \frac{s\,D_{eff,i}}{R_p}\,\frac{\partial \mathrm{Ci,s}\left(t,z,r,r_p\right)}{\partial r_p}\bigg|_{r_p=R_p} \tag{2}$$

Eq. (3) summarizes the mass balance for the solid phase: the state variable is the concentration of component i at the radial and axial locations r and z, respectively and within the catalyst particle at radial location r_p . Similarly to the liquid phase mass balance, the concentration field depends on the effective diffusivity and shape factor and holdups (liquid and solid phase), moreover, the reaction term is included here consisting of catalyst density, ratio of holdups, stoichiometric coefficients and reaction rate.

$$\frac{\partial C_{i,S}\left(t,z,r,r_p\right)}{\partial t} = \frac{D_{eff,i}}{\varepsilon_p}\left(\frac{\partial^2 \mathrm{C}_{i,S}\left(t,z,r,r_p\right)}{\partial {r_p}^2} + \frac{s}{r_p}\,\frac{\partial C_{i,S}\left(t,z,r,r_p\right)}{\partial r_p}\right) + \rho_{cat}\sum\left(\vartheta_{i,j} r_j\left(t,z,r,r_p\right)\frac{\varepsilon_L}{\varepsilon_p}\right) \tag{3}$$

2.1.2. Energy balance

In contrary to the mass balance, where the state variables were the concentrations of the components in each phase, the energy balance is issued to calculate the temperature of each phase. As an analogy to the mass balance, the accumulation term of the gas-phase energy balance is the net sum of the gas liquid heat transfer, convection, as well as axial and radial conduction and dispersion. The gas-phase temperature depends on the axial and radial locations (z and r), and the key parameters include the radial and axial conductivities along with the dispersion coefficients as well as the gas phase velocity and density at the axial and radial directions, as shown in Eq. (4).

$$\frac{\partial T_G(t,z,r)}{\partial t} = \frac{-h_G a}{\rho_G(z,r)\varepsilon_G c_{p,G}}\left(T_G(z,r) - T_L(z,r)\right) - \frac{\partial\left(u_G(z,r)T\mathrm{G}(t,z,r)\right)}{\partial z} + \left(D_{z,G} + \frac{\lambda_{z,G}}{\rho_G(z,r)\varepsilon_G c_{p,G}}\right)\frac{\partial^2 T_G(t,z,r)}{\partial z^2} + \left(\frac{\partial^2 T_G(t,z,r)}{\partial r^2} + \frac{1}{r}\,\frac{\partial T_G(t,z,r)}{\partial r}\right)\left(D_{r,G} + \frac{\lambda_{r,G}}{\rho_G(z,r)\varepsilon_G c_{p,G}}\right) \tag{4}$$

The energy balance of the liquid phase is summarized in Eq. (5), where gas-liquid and liquid-solid heat transfer effects are included. Similarly to the gas phase, the gas-liquid heat transfer, convection and both radial and axial conduction terms are presented, and heir net sum with the heat transfer from the solid phase results to the accumulation term.

$$\frac{\partial T_L(t,z,r)}{\partial t} = \frac{h_G a}{\rho_L \varepsilon_L c_{p,L}}\left(T_G(z,r) - T_L(z,r)\right) - u_L\frac{\partial T_L(t,z,r)}{\partial z} + \left(\frac{\lambda_{z,L}}{\rho_L \varepsilon_L c_{p,L}} + D_{z,L}\right)\frac{\partial^2 T_L(t,z,r)}{\partial z^2} + \left(\frac{\partial^2 T_L(t,z,r)}{\partial r^2} + \frac{1}{r}\,\frac{\partial T_L(t,z,r)}{\partial r}\right)\left(\frac{\lambda_{r,L}}{\rho_L \varepsilon_L c_{p,L}} + D_{r,L}\right) - \frac{s\,\lambda_P}{\rho_L \varepsilon_L c_{p,L}\,Rp}\,\frac{\partial T_S\left(t,z,r,r_p\right)}{\partial r_p}\bigg|_{r_p=R_p} \tag{5}$$

For the solid-phase energy balance, the accumulation term results from the radial heat conduction effect and reaction enthalpies involved, the state variable is the temperature at the radial and axial locations and inside the catalyst particle as written in Eq. (6), where only the particle conductivity was taken into consideration. This assumption motivated with the fact that the detailed heat conduction geometry in trickle bed reactors in the presence of particles with irregular pore structures is difficult to be determined.

$$\frac{\partial T_S(t,z,r,r_p)}{\partial t} = \frac{\lambda_P}{\rho_{cat} c_{p,p}} \left(\frac{\partial^2 T_S(t,z,r,r_p)}{\partial r_p{}^2} + \frac{s}{r_p} \frac{\partial T_S(t,z,r,r_p)}{\partial r_p} \right) + \frac{\varepsilon_L}{\varepsilon_p c_{p,p}} \sum \left((-\Delta H_r) r_j(t,z,r,r_p) \right) \quad (6)$$

Because some reactions, such as the selective oxidation of sugars reported by Kusema et al. [25] require a constant temperature profile, thus a jacket around the reactor was included to insure the desired temperature. The heat transfer between the reactor and the cooling jacket was also taken into consideration as shown in Eq. (7). The fluid flow was assumed to be high enough to maintain its temperature to be constant in all the radial and axial locations as shown in Eq. (8).

$$Q(jacket) = UA(reactor) \int_0^L (T(reactor) - T(jacket)) dz \quad (7)$$

$$\rho_{cooling\ fluid} c_{p,cooling\ fluid} V_{column} \frac{\partial T}{\partial t} = F_{cooling\ fluid} c_{p,cooling\ fluid} (T_{in} - T) + Q \quad (8)$$

As the model is a combination of PDEs (1)–(6), it is of high importance to define the initial and boundary conditions since they have a high impact on both the accuracy of the results and the speed of getting numerical simulation results. The boundary and initial conditions for each phase are shown in detail in Eqs. (9)–(24).

2.1.3. Gas phase boundary conditions

1. Entrance

$$\boldsymbol{C_{i,G}(t,0,r) = C_{i,G\ in}\ T_G(t,0,r) = T_{G\ in}} \quad (9)$$

2. Outlet

$$\left.\frac{\partial C_{i,G}(t,z,r)}{\partial z}\right|_{z=L} = 0\ \left.\frac{\partial T_G(t,z,r)}{\partial z}\right|_{z=L} = 0 \quad (10)$$

3. Centre

$$\left.\frac{\partial C_{i,G}(t,z,r)}{\partial r}\right|_{r=0} = 0\ \left.\frac{\partial T_G(t,z,r)}{\partial r}\right|_{r=0} = 0 \quad (11)$$

4. Wall

$$\left.\frac{\partial C_{i,G}(t,z,r)}{\partial r}\right|_{r=R} = 0\ \left.\frac{\partial T_G(t,z,r)}{\partial r}\right|_{r=R} = 0 \quad (12)$$

2.1.4. Liquid phase boundary conditions

5. Entrance

$$\boldsymbol{C_{i,L}(t,0,r) = C_{i,L\ in}\ T_L(t,0,r) = T_{L\ in}} \quad (13)$$

6. Outlet

$$\left.\frac{\partial C_{i,L}(t,z,r)}{\partial z}\right|_{z=L} = 0\ \left.\frac{\partial T_L(t,z,r)}{\partial z}\right|_{z=L} = 0 \quad (14)$$

7. Centre

$$\left.\frac{\partial C_{i,L}(t,z,r)}{\partial r}\right|_{r=0} = 0\ \left.\frac{\partial T_L(t,z,r)}{\partial r}\right|_{r=0} = 0 \quad (15)$$

8. Wall

$$\left.\frac{\partial C_{i,L}(t,z,r)}{\partial r}\right|_{r=R} = 0 - \lambda_{r,L} \frac{\partial T_L(t,z,r)}{\partial r}|_{r=R} = h_w (T_L(z,R) - T_{wall})) \quad (16)$$

2.1.5. Solid phase boundary conditions

9. Particle centre

$$\left.\frac{\partial C_{i,S}(t,z,r,rp)}{\partial r_p}\right|_{r_p=0} = 0\ \left.\frac{\partial T_S(t,z,r,rp)}{\partial r_p}\right|_{r_p=0} = 0 \quad (17)$$

10. Particle surface

$$\boldsymbol{C_{i,S}(t,z,r,R_p) = C_{i,L}(t,z,r)\ T_S(t,z,r,R_p) = T_L(t,z,r)} \quad (18)$$

11. Entrance

$$\boldsymbol{C_{i,S}(t,0,r,r_p) = C_{i,S\ in}\ T_S(t,0,r,r_p) = T_{S\ in}} \quad (19)$$

12. Outlet

$$\left.\frac{\partial C_{i,S}(t,z,r,r_p)}{\partial z}\right|_{z=L} = 0\ \left.\frac{\partial T\mathrm{L}(t,z,r,r_p)}{\partial z}\right|_{z=L} = 0 \quad (20)$$

13. Centre

$$\left.\frac{\partial C_{i,S}(t,z,r,r_p)}{\partial r}\right|_{r=0} = 0\ \left.\frac{\partial T\mathrm{S}(t,z,r)}{\partial r}\right|_{r=0} = 0 \quad (21)$$

14. Wall

$$\left.\frac{\partial C_{i,S}(t,z,r,r_p)}{\partial r}\right|_{r=R} = 0 - \lambda_{r,L} \frac{\partial T\mathrm{S}(t,z,r,r_p)}{\partial r}|_{r=R} = h_w (T_s(z,R,r_p) - T_{wall})) \quad (22)$$

The boundary conditions for the liquid and gas phases comprise the feed concentrations and temperature at the reactor entrance, as well as their axial and radial derivatives at the reactor outlet and at its centre and wall as shown by the above equations. For the solid phase, besides to the previous conditions, the radial derivatives of the concentrations and temperature at the particle centre in addition to the values of the concentration and temperature at the particle surface are included. The closed boundary conditions of Danckwerts are applied at the reactor outlet, while at the entrance the plug flow condition are used due to the downward gravity of the inlet flows. The initial concentrations of the feed are given below,

$$C_{\mathrm{Arab,G}}(t,z,r) = 0\ \ mol/m^3\ \ C_{\mathrm{Arab,L}}(t,z,r) = C_{\mathrm{Arab,S}}(t,z,r,rp) = 0.7.10^3\ mol/m^3 \quad (23)$$

$$C_{O_2,\mathrm{L}}(t,z,r) = C_{O_2,\mathrm{S}}(t,z,r,rp) = 0\ \ mol/m^3\ \ C_{O_2,\mathrm{G}}(t,z,r,rp) = 0.1012\ mol/m^3 \quad (24)$$

$$T_s(t,z,r,rp) = T_L(t,z,r) = T_G(t,z,r) = 70 + 273\ K \quad (25)$$

The initial conditions are summarized in Eqs. (23)–(25). In our case for the application and validation purposes, the selective oxidation of arabinose reported in the articles of Herrero Manzano et al. and Kusema et al. [25,26] was taken as a demonstration case, thus the values above were extracted from the work of Herrero Manzano et al. (2021) [26] . The objective is to compute the conversion rate of arabinose, the concentration profiles of the different species and the temperature profile inside the trickle bed reactor.

2.2. Parameter estimations

In the mass and energy balances, the some of the key parameters were calculated using well established correlations. The catalyst shape

factor appears in the mass and energy balances of the catalyst particle. The particle geometry was taken into consideration [27] by using Eq. (26) proposed by Salmi et al. [28], where V_p and A_p are the volume and the outer surface area of the catalyst particle respectively. It should be noticed that non-integer numbers of the shape factor can appear for particles deviating from ideal geometry (long cylinder, sphere, slab)

$$s = 1 + R_p \frac{Ap}{Vp} \tag{26}$$

One of the key parameters to be estimated are the molecular and effective diffusivities. The molecular diffusivity is calculated using Wilke-Chang correlation [29], while the effective diffusivity is obtained by correcting the molecular diffusivity by the ratio of tortuosity and porosity, in our case more accurate values are reported in ref. [26] . Concerning the liquid viscosity, which is required for the estimation of Reynolds number, the correlation adopted in Eq. (27) was based on arabinose hydrogenation previous studies [30] and taking into account the dependence of the viscosity on both temperature and arabinose mass fraction x_a.

$$\eta_{fluid} = 10^{-3} exp\left(\frac{1.54x_a}{T_{L\,in} - 273} + 3.81.10^{-4}x_a^2 - 1.10.10^{-2}x_a - 2.85 + \frac{194}{T_{L\,in} - 273} - \frac{3890}{(T_{L\,in} - 273)^2}\right) \tag{27}$$

The gas-liquid mass transfer coefficient is included in the mass balance as shown in Eqs. (1) and (2). Eq. (28) extracted from ref. [11] was adopted here. The correction factor γ was included to take into consideration the inaccuracy of the gas-liquid mass transfer coefficient as reported in ref. [19]. The expressions for various dimensionless numbers are summarized in Table 1.

$$k_{iL}a = 0.45\gamma\left(\frac{d_K}{{d_K}^2}\right)\left({X_G}^{0.65}{Re_L}^{1.04}{We_L}^{0.26}{Sc_L}^{0.65}\right)\left(\frac{a_{sp}\,d_K}{1-\varepsilon_p}\right)^{0.325} \tag{28}$$

Peclet number is a dimensionless quantity used in axial and radial dispersion models for non-dimensionalisation of analytical and numerical solutions. It reflects the characteristic ratio of convective transport rate to diffusive and dispersive transport rate [31], also it is beneficial to retain it for solution stability for numerical solutions. Among the existing correlations used to compute the Peclet number the most popular is the Chung and Wen correlation [32] it is quite popular since it used large amounts of experimental data to generate it; in 1970 De Ligny [33] improved the correlation by including molecular diffusion.

The axial dispersion coefficients for the liquid phase are usually obtained experimentally with the aid of inert tracers. In our laboratory, across the years, numerous experiments have been performed which has guided us to estimate the order of magnitude of the axial dispersion coefficient, while the radial dispersion is typically less profound and thus often neglected in classical dispersion models. The axial dispersion coefficient was in the current case calculated using the Peclet number as shown in Eqs. (29)–(30), while the radial dispersion coefficient was taken equal to one third of the axial one as shown in the Eqs. (31)–(32) following the considerations reported previously [19]. According to our previous work [21,34] the order of magnitude of the liquid phase Peclet number was 2–10, while for the gas phase the Peclet number can reach 100,because the flow pattern might approach plug flow with an excess of gas flow. For numerical simulations, the liquid-phase Peclet number was taken 10 indicating some degree of backmixing.

Table 1
Dimensionless numbers appearing in the model.

Dimensionless numbers	Expression
Reynolds number for liquid phase	$Re_L = \frac{u_L\,\rho_L}{\eta_{fluid}}$
Schmidt number for liquid phase	$Sc_L = \frac{\eta_{fluid}}{\rho_L D_L}$
Weber number for liquid phase	$We_L = \frac{2R_p\rho_L u_L}{\sigma_L}$
Modified Lockhart Martinelli number	$X_G = \frac{u_G}{u_L}\sqrt{\frac{\rho_g}{\rho_L}}$

$$D_z = u_L.\frac{L}{Pe_L} \tag{29}$$

$$D_{z,G}(z,r) = u_G(z,r).\frac{L}{Pe_G} \tag{30}$$

$$D_r = \frac{D_z}{3} \tag{31}$$

$$D_{r,G} = \frac{D_{z,G}(z,r)}{3} \tag{32}$$

The gas phase velocity is calculated using Eq. (34) where the cross section area A is constant and that gas molar flow F_G stays constant since the liquid phase is saturated with O_2 already.

$$C_G(z,r) = \frac{F_G}{A^* u_G(z,r)} \text{ at t} \neq 0 \text{ and } C_{Gin} = \frac{F_G}{A^* u_G 0} \text{ at } t = 0 \tag{33}$$

After dividing the previous equation with the value at t = 0 we find

$$u_G(z,r) = u_{G,0}\,\frac{C_{Gin}}{C_G(z,r)} \tag{34}$$

The pressure drop was calculated using the correlation proposed by Ellman et al. (1988) [35] shown in Eq. (35) which has also been reported by Degirmenci and Rebrov (2019) [36]. The choice of such a correlation was driven by its has application range (0.1–10 MPa) and also by the fact that the pressure drop along the whole reactor was not influenced by the gas flow rate, thus the residence time and the liquid holdup at steady state remained unchanged either starting from a fully liquid-filled or fully gas-filled reactor [35,36] .

$$\frac{\Delta P(z,r)}{L} = \frac{\rho_G}{R_p}u_G(z,r)^2\left(200\,(\xi X_G(z,r))^{-1.2} + 85(\xi X_G(z,r))^{-0.5}\right) \tag{35}$$

where $\xi = \frac{{Re_L}^2}{0.001 + {Re_L}^{1.5}}$

Noteworthy, to have a more accurate pressure drop calculation, Eq. (35) can be replaced by a corresponding differential equation and then solved together with mass and energy balances. However, for the sake of simplification, our case study was focusing on arabinose oxidation which is performed under atmospheric pressure and thus the pressure is maintained virtually constant, and the pressure drop term is included in the model.

The liquid hold up can be calculated using the correlation proposed by Lange et al. (2005) [37] . However, for very low liquid velocities, the liquid holdup is a weak function of the Reynolds number being constant and practically independent of the gas-phase Reynolds number, and thus for the verification, the typical value of 0.3 was adopted. The bed porosity $\varepsilon_B$was taken equal 0.4 for extrudates and 0.35 for powder as reported by Ranade et al. (2011) [11] and therefore the solid phase liquid holdup is easily calculated using Eq. (36).

$$\varepsilon_p + \varepsilon_B = 1 \tag{36}$$

2.3. Basic assumptions

The combination of heat and mass transfer and heat conduction in the presence of catalyst particles with irregular shapes makes the rigorous modelling of three-phase catalytic trickle bed reactors a complicated task, thus some simplifications are introduced and some assumptions become inevitable.

In the present it was assumed that the wall is completely wet and the

initial liquid feed is well distributed by the means of a fine sand bed distributor and the liquid-phase velocity remains constant, also the catalyst distribution in the bed was supposed to be uniform, and finally, all the three phases coexist everywhere in the reactor bed [19]. Also, it is worth mentioning that according to ref. [37], the holdup at low interaction regimes is a weak function of the Reynolds number and thus it can be considered constant.

2.4. Reaction kinetics

The reaction stoichiometry of the selective arabinose oxidation to arabinoic acid on gold catalyst is shown in Eq. (37). The reaction kinetics has been extensively studied previously [25,26,38]. The kinetics was described using a classical Langmuir–Hinshelwood rate equation displayed in Eqs. (38)–(39), but including a deactivation factor a which describes the disappearance of the active sites because of leaching of the active metal as described by Eq. (40), where α t is an empirical exponent and C_{00} denotes the total concentration of active sites at time moment t; for simulation purposes the case of $C_{00} = 1$ is considered. The kinetic expression and the numerical values were adopted from ref. [26], where the rate constant was calculated using Arrhenius law as shown in Eq. (40).

$$\text{Arabinose} + \frac{1}{2}O_2 \rightarrow \text{Arabinoic Acid} \tag{37}$$

$$r(t,z,r,r_p) = a^2 \frac{k(t,z,r,rp) f_{active} C_{O2,s}(t,z,r,r_p) C_{Ara,s}(t,z,r,r_p)}{1 + K_{ara} C_{Ara,s}(t,z,r,r_p) + K_{O2} C_{O2,s}(t,z,r,r_p)} \tag{38}$$

$$k(t,z,r,rp) = A.exp\left(-\frac{Ea}{R}\left(\frac{1}{T_s(t,z,r,rp)} - \frac{1}{T_{ref}}\right)\right) \tag{39}$$

$$\frac{da}{dt} = -kC_{00}{}^{\alpha-1}(a-a^*)^{\alpha} \tag{40}$$

2.5. Numerical strategy

The software gProms was used for the simultaneous numerical solution of the model equations. gProms is a custom modelling and simulation environment applied mainly on the modelling, design and optimization of chemical processes. It is developed by Process Systems Enterprise, which has its roots in the Department of Chemical Engineering at Imperial College in London, UK. The numerical method of lines was used, which involves the discretisation of the distributed system with respect for the all the spatial domains to transform a systems of integral, partial and ordinary differential, and algebraic equations (IPDAEs) to a set of differential algebraic equations (DAEs) [39]. The numerical methods of lines is known to work quite well with scalars. The discretization method used in this work was centred finite difference method (CFDM).

3. Simulation results and discussion

3.1. Effect of catalyst shape and size on conversion at the reactor outlet

The dynamic model of the trickle bed reactors developed in this work was applied to describe arabinose oxidation in the presence of gold catalyst. The oxidation rate expression and catalyst characteristics were adapted from ref. [26] .The physical properties and reactor characteristics are listed in Table 2.

The effects of the variation of the catalyst particle shape and size are illustrated in Fig. 1, where a decrease of the conversion rate is observed when increasing the particle size, which is due to the fortification of the mass transfer resistance, i.e. slow mass transfer inside the catalyst particles and also existence of external mass transfer limitations around the particles. High conversion rate of arabinose is achieved for the small

Table 2
List and values of parameters used in the TBR simulation.

Parameters	Value	Unit	Refernces
ρ_{cat}: Catalyst density	424	kg/m^3	[19]
ρ_L: Density of liquid phase	950	kg/m^3	[19]
m(O_2): Molar mass of oxygen	32	g/mol	[19]
σ_{H2O}: Surface tension of water	72.8 10^{-3}	N/m	[19]
η_{H2O}: Viscosity of water	0.2 10^{-3}	Pa s	[19]
$C_{p,\,cat}$: Specific heat of catalyst	3000	J/kg K	[19]
$C_{p,\,L}$: Specific heat of liquid phse	4300	J/kg K	[19]
$C_{p,\,G}$: Specific heat of gas phase	918	J/kg K	[19]
α: Exponent in catalyst activity function	1		[26]
a*:Limiting activity factor	0.47282		[26]
A: Arrhenius constant	53.99	m^6/mol kgcat	[26]
Pe_L: Peclet number of liquid phase	10		[19]
Pe_G: Peclet number of gas phase	100		[19]
$\lambda_{r,\,L}$: Radial heat conductivity of liquid phase	2	W/ K m	[19]
$\lambda_{r,\,G}$: Radial heat conductivity of gas phase	0.1	W/ K m	[19]
$\lambda_{z,\,L}$: Axial heat conductivity of liquid phase	2	W/ K m	[19]
$\lambda_{z,\,G}$: Axial heat conductivity of gas phase	0.1	W/ K m	[19]
λ_p: Particle heat conductivity	0.5	W/ K m	[19]
$(-\Delta H_r)$: Reaction enthalpy	32.94.10^3	J/mol	Calculated using Aspen Plus
h_Ga: Gas–liquid heat transfer coefficient	1,000,000	W/ K m^3	[19]
h_w: Wall heat transfer coefficient	1000	W/ m^2 K	[19]
D_L: Diffusivity of Arabinose in water	4 10^{-8}	m^2/s	[26]
Effective diffusivity (D_{eff}) of Arabinose	2.474 10^{-9}	m^2/s	[26]
Effective diffusivity (D_{eff}) of O_2	9.851 10^{-9}	m^2/s	[26]
Effective diffusivity (D_{eff}) of Arabinoic Acid	2.403 10^{-9}	m^2/s	[26]
CO_2S:Saturation concentration of oxygen	0.103	mol/m^3	[26]
L: Reactor length	0.5	m	
R: Reactor radius	5	cm	

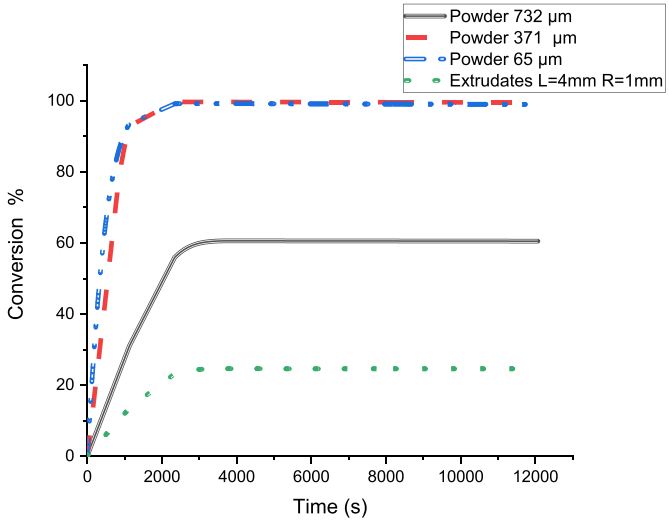

Fig. 1. Effect of catalyst shape and size on the conversion of arabinose at the reactor outlet.

powder sizes (65 and 371 μm), while for the extrudates it remains at ca. 25% and ca.60% for catalyst powder with average size of 732 μm. The same trend of the effect of the same powder size and extrudates is observed experimentally in the work of Herrero Manzano et al. [26] with the sole exception is the extrudates eventually have higher conversion rate due to the use of special device that supresses external mass transfer.

The concentrations of the different species across the time in the liquid phase are shown in detail in Figs. 2–5. The steady state oxygen concentration remains constant 0.102 mol/m^3 and is thus very small in comparison to the arabinose and arabinoic acid concentrations, which goes along with real life situation; in fact, in larger scale, air is used instead of oxygen in the oxidation processes and in our case the atmospheric pressure is applied because thus it is easy to control the gas phase flow.

In Figs. 2–3, the reaction is limited by the consumption of the reactant, arabinose, and the steady state conversion is reached faster than for larger particles which is due to the suppression of mass transfer resistance. However, the steady state and complete conversion of arabinose is reached slightly faster for the 371 μm powder catalyst than for the smallest one, which might be due to the fact that for really small particles the instability of the catalyst can be an issue [40] in addition to the eventual numerical instability that should be taken into account.

For larger particles, e.g. Figs. 4 and 5, complete conversion is not achieved at the reactor outlet instead, the concentration of arabinoic acid is varying lot (ca. 42 m^3/mol vs 17 m^3/mol), however the reaction reaches the steady state simultaneously but with a slower dynamics comparing with smaller particles. The pressure drop was very low (ca. 0 bar), which is expected in this case study, where the reaction is carried out in atmospheric pressure.

3.2. Effect of location, catalyst shape and size

The arabinose conversion and temperature profiles across the radial and axial position for each catalyst size and shape are shown in Fig. 6.

The conversion was investigated across the reactor as a function of time as shown in Fig. 6: the conversion is proportional to both the simulation time and the axial position. It is however observed that the axial position influences the conversion more compared to the simulation time.

In contrast to the axial location effect, Fig. 7 reveals that the radial position has a small effect on the conversion rate comparing to the axial

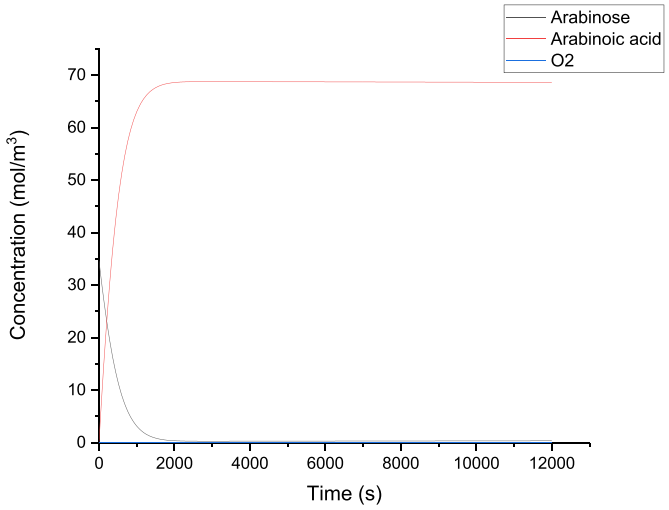

Fig. 2. Concentrations of different species at the reactor outlet using powder catalyst (65 μm).

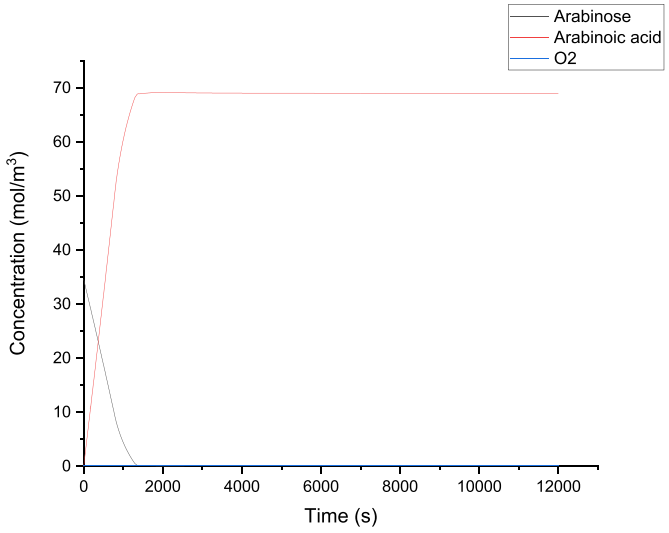

Fig. 3. Concentration of different species at the reactor outlet using powder catalyst (371 μm).

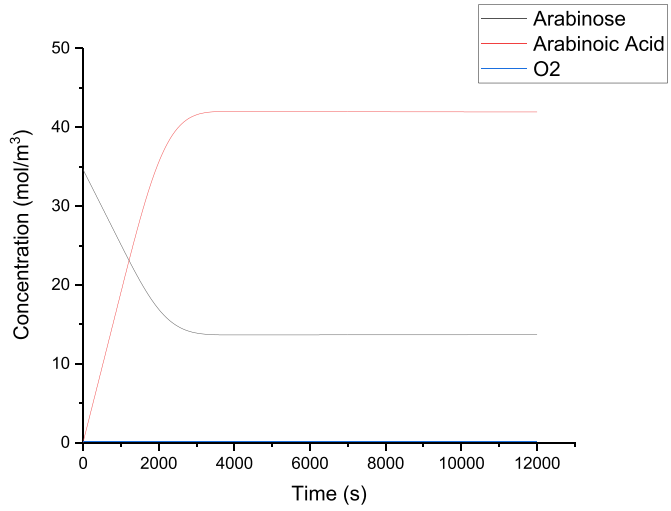

Fig. 4. Concentrations of different species at the reactor outlet using powder catalyst (732 μm).

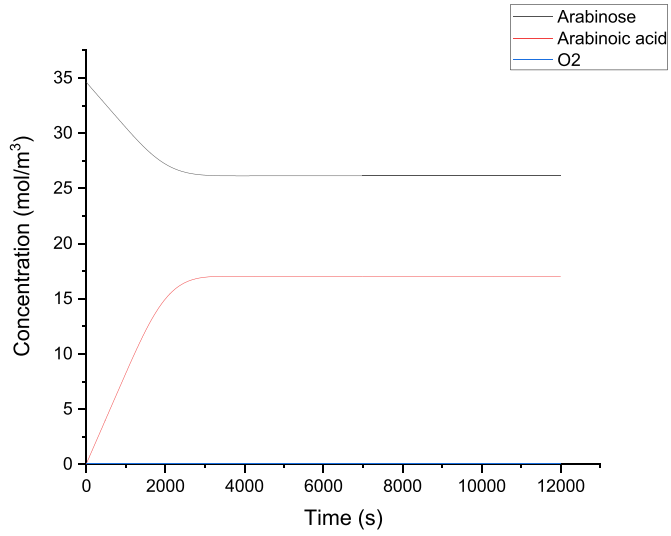

Fig. 5. Concentrations of different species at the reactor outlet using catalyst extrudates (l = 4 mm and r = 1 mm).

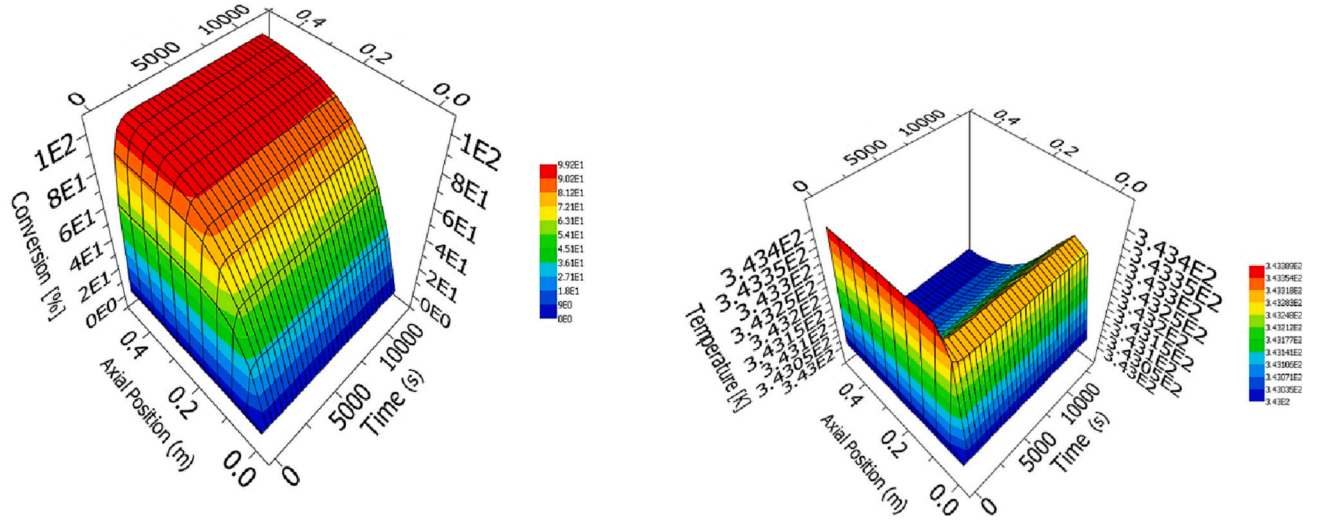

Fig. 6. Effect of axial position on the conversion rate and temperature (powder 65 μm) at reactor centre.

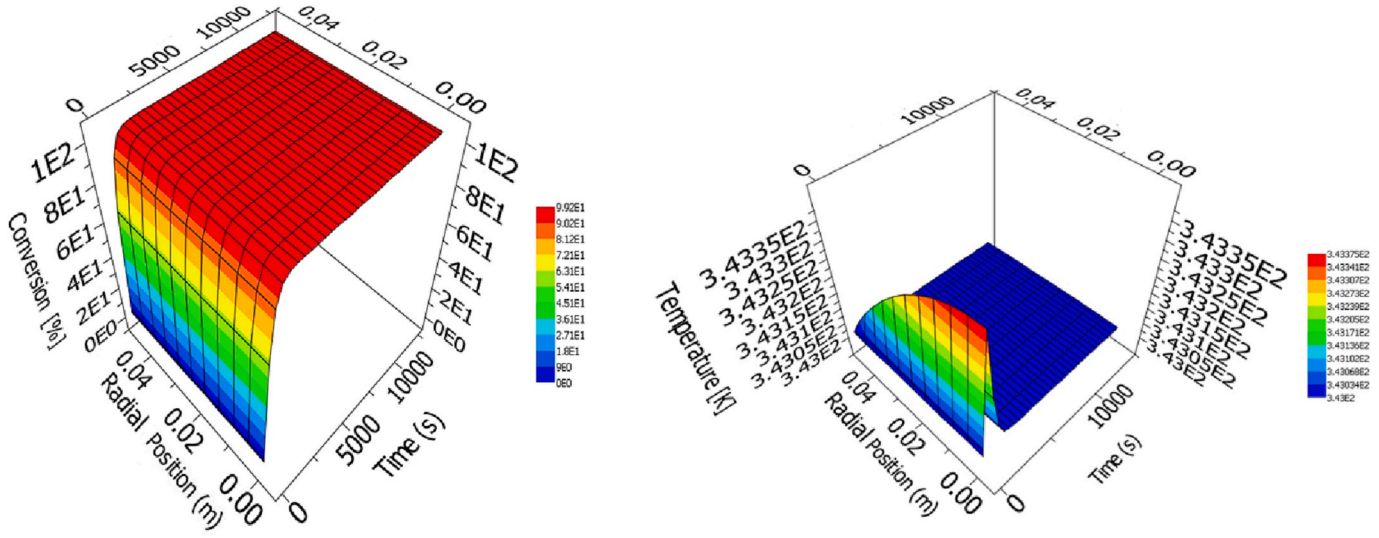

Fig. 7. Effect of radial position on conversion rate and temperature at reactor outlet (powder 65 μm).

one. In fact, across the radial positions, the same conversion rate behaviour as a function of time is observed: a practically linear increase until reaching the maximum value of the sugar conversion at steady state.

Figs. 8 and 9 summarize the effect of both axial and radial positions on the dynamic conversion at the reactor outlet and centre for the bigger particle size (371 μm). The results are similar to the previous case, because almost complete conversion is achieved at the steady state. However, when looking more closely at the simulated results, more time and shorter reactor is needed to achieve the steady state at both the reactor outlet and the centre. Comparing to the previous case, complete conversion is observed before the reactor outlet and thus for this powder catalyst the almost complete conversion is achieved using a shorter bed.

For the simulations presented in Figs. 10 and 11 the catalyst size was increased more (731 μm). In contrary to the previously mentioned cases, the conversion is limited to ca. 60%. Fig. 11 shows that the radial position has no effect on the conversion rate and that the steady state is achieved more slowly compared to than previous cases. The axial position, on the other hand, has a higher effect on the conversion rate as revealed in Fig. 10 and the steady state is not achieved at the reactor outlet even by increasing the simulation time.This observation suggests that a longer bed is required to increase the conversion rate.

The effect of the catalyst shape was investigated numerically, by similarity to the behaviour of cylindrical extrudates. The obtained results are summarized in Figs. 12 and 13, which are similar to the previous cases. The maximum conversion was ca. 25% which is lower than for the powder. Similarly to the previous case, Fig. 12 shows that the steady state is not reached while it is attained in Fig. 13; thus the conversion rate can be increased by increasing the length of the reactor only.

The simulation results of the energy balance for all the studied cases are summarized in the temperature profiles shown in Figs. 6–13. Various trends were observed, in fact both single peaks and steady state are observed in the figures. However, the temperature difference between the highest and lowest value are less than 14 K which confirms the isothemal conditions of the reaction and is in agreement with experimental findings of [26].

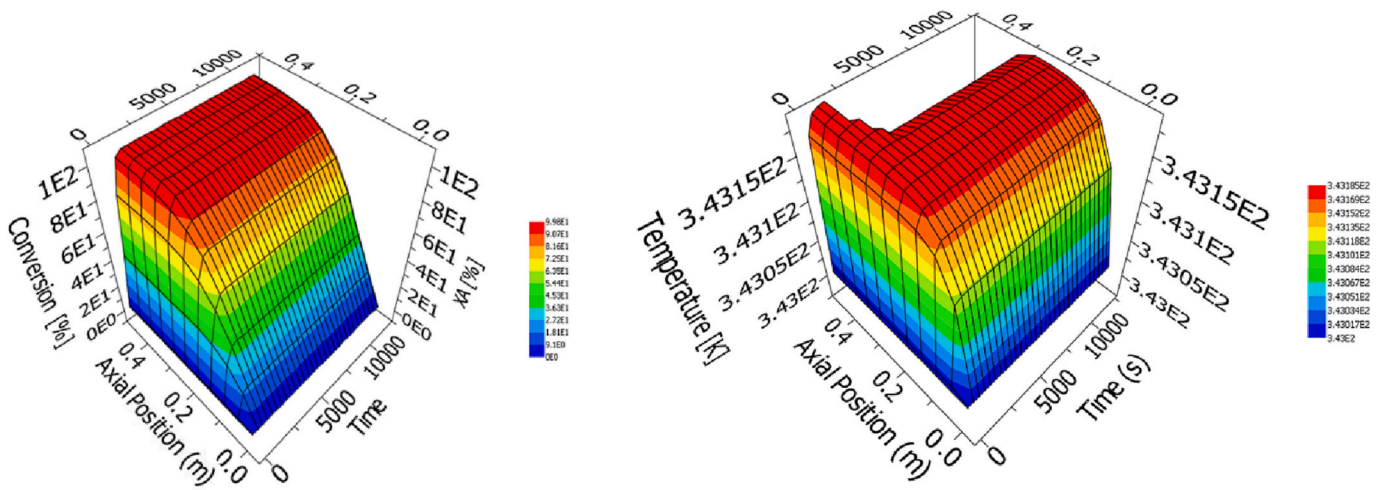

Fig. 8. Effect of axial position on conversion and temperature at reactor outlet (powder 371 μm).

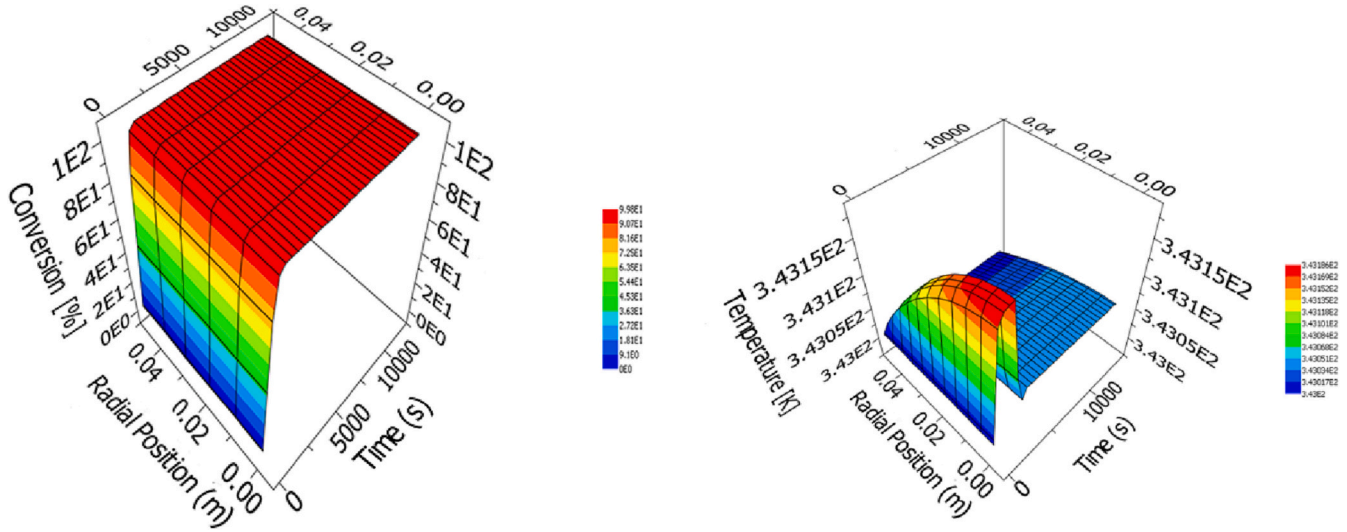

Fig. 9. Effect of radial position on conversion and temperature at reactor outlet (powder 371 μm).

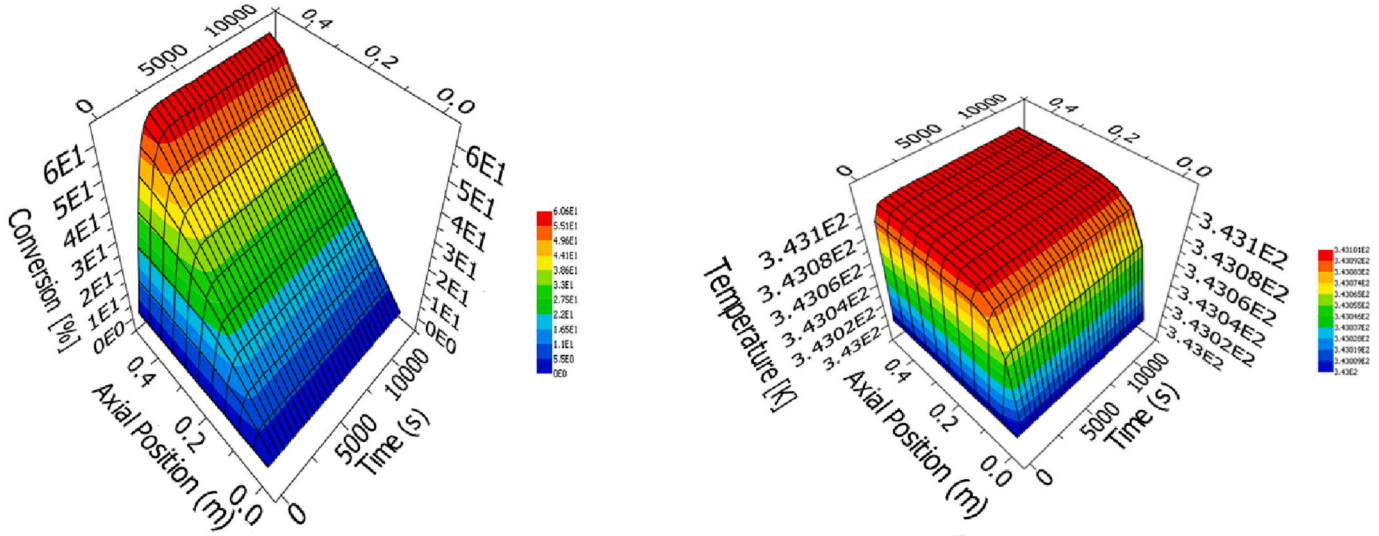

Fig. 10. Effect of axial position on the conversion and temperature at reactor centre (powder 732 μm).

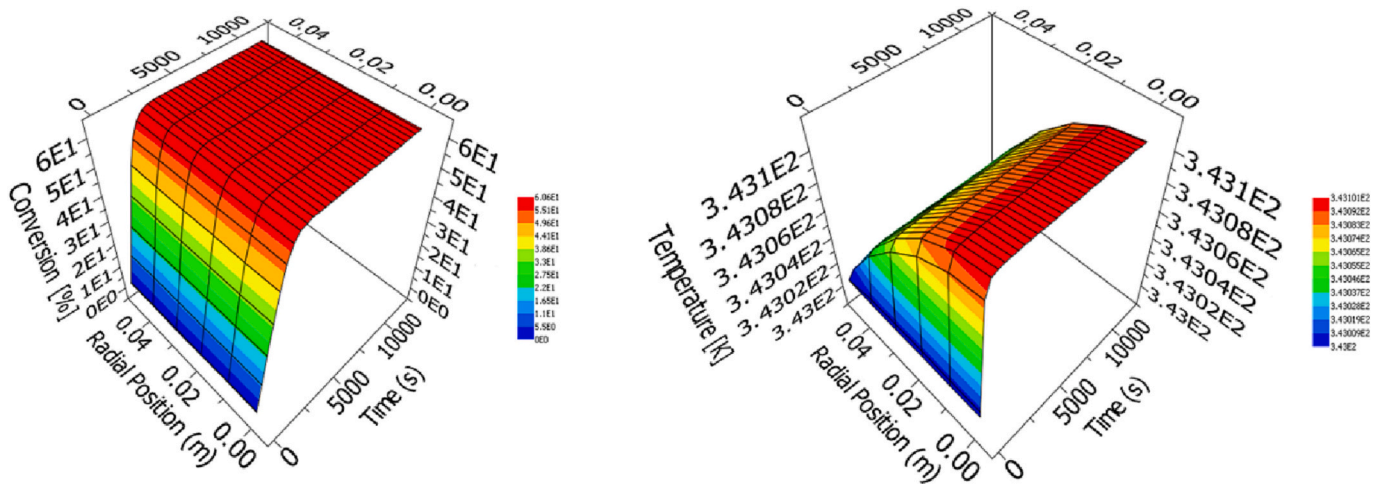

Fig. 11. Effect of radial position on the conversion and temperature at reactor outlet (powder 732 μm).

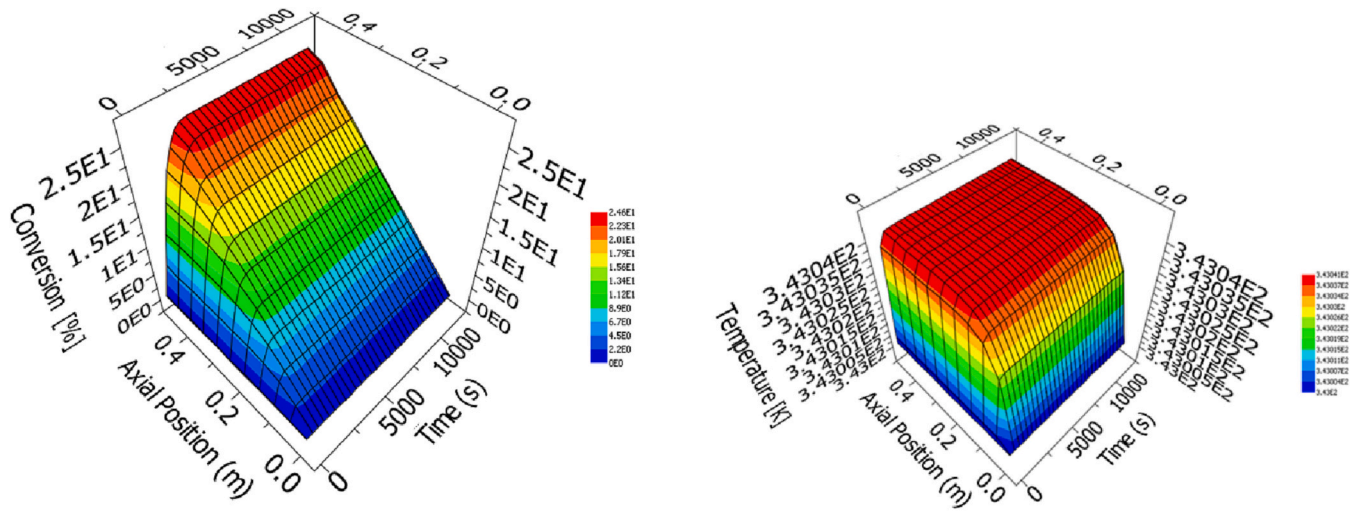

Fig. 12. Effect of axial position on conversion and temperature at reactor centre (extrudates).

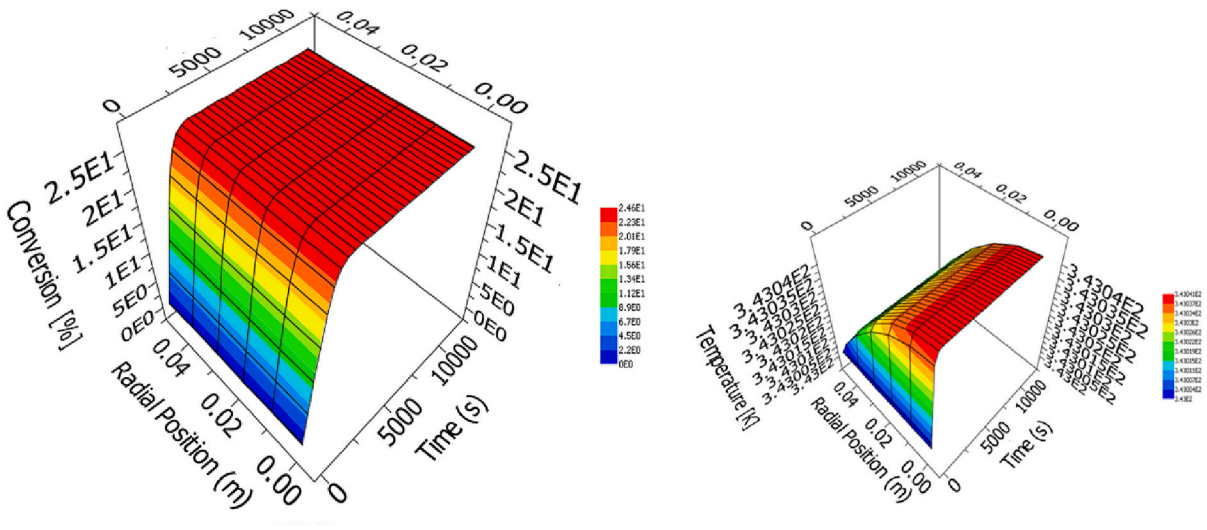

Fig. 13. Effect of radial position on the conversion and temperature at reactor outlet (extrudates).

4. Conclusions

The main objective of this work was to develop a general and dynamic model for three-phase trickle bed reactors. The model includes an extensive amount of elements to take into account all the major effects and to be as general as possible so that the model can be used as a framework for other reaction system in future.

For the case study, arabinose oxidation, the results showed that the maximum reactant conversion depends strongly on the size of the catalyst particle. The smallest catalyst particle size (65 μm) allows a rapid conversion but required a relatively long reactor, while for the larger particles (371 μm) the process is a bit slower because of mass transfrer limitations. The other catalyst sizes and shapes did not give a complete reactant conversion at the reactor outlet. However, the simulated profiles indicated that a high conversion can be achieved for a much longer reactor.

The obtained results illustrate a quite interesting modelling stability that might pave the way to the investigation of a sound scale up by including multiscale heat transfer correlations and analysing the life cycle of various reaction systems in a larger scale, although more accurate simulations might require further kinetic and flow experiments using trickle bed reactors.

Declaration of Competing Interest

The authors have declared no conflict of interest.

Data availability

Data will be made available on request.

Acknowledgments

This work is part of the activities of the Åbo Akademi Process Chemistry Centre (PCC) and financed by the Academy of Finland, the Academy Professor grants 319002 (T. Salmi). The economic support obtained from the Finnish Cultural Foundation (SKR), Walter Ahlstrom Foundation, and from The Society of Swedish Literature in Finland (SLS) is gratefully acknowledged (M. Hachhach).

References

[1] F. Cherubini, The biorefinery concept: using biomass instead of oil for producing energy and chemicals, Energy Convers. Manag. 51 (2010) 1412–1421, https://doi.org/10.1016/j.enconman.2010.01.015.
[2] Y.H.P. Zhang, Reviving the carbohydrate economy via multi-product lignocellulose biorefineries, J. Ind. Microbiol. Biotechnol. 35 (2008) 367–375, https://doi.org/10.1007/S10295-007-0293-6.
[3] T.H. Mekonnen, M. Misra, A.K., Mohanty, Processing, performance, and applications of plant and animal protein-based blends and their biocomposites, in: Biocomposites Des. Mech. Perform, Elsevier Inc., 2015, pp. 201–235, https://doi.org/10.1016/B978-1-78242-373-7.00017-2.
[4] M. Hachhach, D.A. Sladkovskiy, T. Salmi, D.Y. Murzin, Selective oxidation of arabinose on gold catalysts: process design and techno-economic assessment, Chem. Eng. Technol. (2021) 1–9, https://doi.org/10.1002/ceat.202100211.
[5] N. Ahmad, M.R. Zakaria, Oligosaccharide from hemicellulose, in: Lignocellul. Futur. Bioeconomy, Elsevier, 2019, pp. 135–152, https://doi.org/10.1016/B978-0-12-816354-2.00008-6.
[6] P. Mäki-Arvela, T. Salmi, B. Holmbom, S. Willför, D.Y. Murzin, Synthesis of sugars by hydrolysis of hemicelluloses - a review, Chem. Rev. 111 (2011) 5638–5666, https://doi.org/10.1021/cr2000042.
[7] T. Mehtiö, M. Toivari, M.G. Wiebe, A. Harlin, M. Penttilä, A. Koivula, Production and applications of carbohydrate-derived sugar acids as generic biobased chemicals 36 (2015) 904–916, https://doi.org/10.3109/07388551.2015.1060189.
[8] I. Grand View Research, Glucaric Acid Market Size Worth. https://www.grandviewresearch.com/press-release/global-glucaric-acid-market, 2017 (accessed December 24, 2021).
[9] C. Wu, X. Tu, Biological and fermentative conversion of syngas, in: Handb. Biofuels Prod. Process. Technol. Second Ed., 2016, pp. 335–357, https://doi.org/10.1016/B978-0-08-100455-5.00012-6.
[10] K.T. Klasson, M.D. Ackerson, E.C. Clausen, J.L. Gaddy, Bioconversion of synthesis gas into liquid or gaseous fuels, Enzym. Microb. Technol. 14 (1992) 602–608, https://doi.org/10.1016/0141-0229(92)90033-K.
[11] V. Ranade, R. Chaudhari, P.R. Gunjal, Trickle Bed Reactors, Elsevier, 2011, https://doi.org/10.1016/C2009-0-16553-4.
[12] D. Li, Z. Li, W. Li, Q. Liu, Z. Feng, Z. Fan, Hydrotreating of low temperature coal tar to produce clean liquid fuels, J. Anal. Appl. Pyrolysis 100 (2013) 245–252, https://doi.org/10.1016/J.JAAP.2013.01.007.
[13] M.P. Dudukovic, F. Larachi, P.L. Mills, Multiphase reactors - revisited, Chem. Eng. Sci. 54 (1999) 1975–1995, https://doi.org/10.1016/S0009-2509(98)00367-4.
[14] Z.V. Kuzeljevic, M.P. Dudukovic, Computational modeling of trickle bed reactors, Ind. Eng. Chem. Res. 51 (2012) 1663–1671, https://doi.org/10.1021/ie2007449.
[15] S.T. Sie, R. Krishna, Process development and scale up: III. Scale-up and scale-down of trickle bed processes, Rev. Chem. Eng. 14 (1998) 203–252, https://doi.org/10.1515/REVCE.1998.14.3.203.
[16] J. Dias Da Silva, Numerical Modelling for a Catalytic Trickle-Bed Reactor Using Laplace Transform Technique 43, 2015, https://doi.org/10.3303/CET1543263.
[17] G.M. Monsalve-Bravo, H.M. Moscoso-Vasquez, H. Alvarez, Scaleup of batch reactors using phenomenological-based models, Ind. Eng. Chem. Res. 53 (2014) 9439–9453, https://doi.org/10.1021/ie500587r.
[18] X. Fan, D. Li, X. Feng, H. Dong, X. Liu, Y. Dan, H. Zheng, A. Fan, W. Li, Modelling and simulation of industrial trickle bed reactor hydrotreating for whole fraction low-temperature coal tar simultaneous hydrodesulfurisation and hydrodenitrification, Fuel. 269 (2020), 117362, https://doi.org/10.1016/J.FUEL.2020.117362.
[19] V. Russo, T. Kilpiö, M. Di Serio, R. Tesser, E. Santacesaria, D.Y. Murzin, T. Salmi, Dynamic non-isothermal trickle bed reactor with both internal diffusion and heat conduction: sugar hydrogenation as a case study, Chem. Eng. Res. Des. 102 (2015) 171–185, https://doi.org/10.1016/j.cherd.2015.06.011.
[20] M.R. Khadilkar, Y.X. Wu, M.H. Al-Dahhan, M.P. Dudukovic, M. Colakyan, Comparison of trickle-bed and upflow reactor performance at high pressure: model predictions and experimental observations, Chem. Eng. Sci. 51 (1996) 2139–2148, https://doi.org/10.1016/0009-2509(96)00071-1.
[21] D. Durante, T. Kilpiö, P. Suominen, V.S. Herrera, J. Wärnå, P. Canu, T. Salmi, Modeling and simulation of a small-scale trickle bed reactor for sugar hydrogenation, Comput. Chem. Eng. 66 (2014) 22–35, https://doi.org/10.1016/j.compchemeng.2014.02.025.
[22] A.M. Dashliborun, F. Larachi, Tracer dispersion in trickle beds under tilts and roll motions – CFD study and experimental validation, Chem. Eng. J. 386 (2020), 122845, https://doi.org/10.1016/J.CEJ.2019.122845.
[23] J. Roininen, V. Alopaeus, S. Toppinen, J. Aittamaa, Modeling and simulation of an industrial trickle-bed reactor for benzene hydrogenation: model validation against plant data, Ind. Eng. Chem. Res. 48 (2009) 1866–1872, https://doi.org/10.1021/IE801411N.
[24] A. Alvarez, J. Ancheyta, Modeling residue hydroprocessing in a multi-fixed-bed reactor system, Appl. Catal. A Gen. 351 (2008) 148–158, https://doi.org/10.1016/J.APCATA.2008.09.010.
[25] B.T. Kusema, J.-P.P. Mikkola, D.Y. Murzin, Kinetics of L-arabinose oxidation over supported gold catalysts with in situ catalyst electrical potential measurements, Catal. Sci. Technol. 2 (2012) 423–431, https://doi.org/10.1039/c1cy00365h.
[26] M. Herrero Manzano, K. Eranen, A. Freites Aguilera, J. Warnå, S. Franz, M. Peurla, J.G. Serna, D. Murzin, T. Salmi, Interaction of intrinsic kinetics, catalyst durability and internal mass transfer in the oxidation of sugar mixtures on gold nanoparticle extrudates, Ind. Eng. Chem. Res. 60 (2021) 6483–6500, https://doi.org/10.1021/acs.iecr.0c05305.
[27] R. Aris, On shape factors for irregular particles-I. the steady state problem. Diffusion and reaction, Chem. Eng. Sci. 6 (1957) 262–268, https://doi.org/10.1016/0009-2509(57)85028-3.
[28] T. Salmi, J.-P. Mikkola, J. Wärnå, Chemical Reaction Engineering and Reactor Technology, Chapman and Hall/CRC, 2019, https://doi.org/10.1201/9781315200118.
[29] C.R. Wilke, P. Chang, Correlation of diffusion coefficients in dilute solutions, AICHE J. 1 (1955) 264–270, https://doi.org/10.1002/aic.690010222.
[30] V. Sifontes Herrera, Hydrogenation of L-Arabinose, D-Galactose, D-Maltose and L-Rhamnose, Åbo Akademi - Åbo Akademi University, 2012. https://www.doria.fi/handle/10024/76669 (accessed May 26, 2021).
[31] S.O. Rastegar, T. Gu, Empirical correlations for axial dispersion coefficient and Peclet number in fixed-bed columns, J. Chromatogr. A 1490 (2017) 133–137, https://doi.org/10.1016/J.CHROMA.2017.02.026.
[32] S.F. Chung, C.Y. Wen, Longitudinal dispersion of liquid flowing through fixed and fluidized beds, AICHE J. 14 (1968) 857–866, https://doi.org/10.1002/AIC.690140608.
[33] C.L. de Ligny, Coupling between diffusion and convection in radial dispersion of matter by fluid flow through packed beds, Chem. Eng. Sci. 25 (1970) 1177–1181, https://doi.org/10.1016/0009-2509(70)85007-2.
[34] T. Kilpiö, Mathematical Modeling of Laboratory Scale Three-Phase Fixed Bed Reactors, Åbo Akademi University, 2013. https://www.doria.fi/handle/10024/92182 (accessed May 27, 2021).
[35] M.J. Ellman, N. Midoux, A. Laurent, J.C. Charpentier, A new, improved pressure drop correlation for trickle-bed reactors, Chem. Eng. Sci. 43 (1988) 2201–2206, https://doi.org/10.1016/0009-2509(88)87104-5.
[36] V. Degirmenci, E.V. Rebrov, Design of catalytic micro trickle bed reactors, De Gruyter (2019), https://doi.org/10.1515/psr-2015-0018.
[37] R. Lange, M. Schubert, T. Bauer, Liquid holdup in trickle-bed reactors at very low liquid Reynolds numbers, Ind. Eng. Chem. Res. 44 (2005) 6504–6508, https://doi.org/10.1021/ie048906r.

[38] B.T. Kusema, B.C. Campo, P. Mäki-Arvela, T. Salmi, D.Y. Murzin, Selective catalytic oxidation of arabinose - a comparison of gold and palladium catalysts, Appl. Catal. A Gen. 386 (2010) 101–108, https://doi.org/10.1016/j.apcata.2010.07.037.
[39] M. Oh, Modelling and simulation of combined lumped and distributed processes, PQDT - UK Irel. 1 (1995). http://login.proxy.library.vanderbilt.edu/login?url=http://search.proquest.com/docview/1780574456?accountid=14816%5Cnhttp://sfx.library.vanderbilt.edu/vu?url_ver=Z39.88-2004&rft_val_fmt=info:ofi/fmt:kev:mtx:dissertation&genre=dissertations+%26+theses&sid.
[40] D.J.S. Sandbeck, N.M. Secher, F.D. Speck, J.E. Sørensen, J. Kibsgaard, I. Chorkendorff, S. Cherevko, Particle size effect on platinum dissolution: considerations for accelerated stability testing of fuel cell catalysts, ACS Catal. 10 (2020) 6281–6290, https://doi.org/10.1021/ACSCATAL.0C00779.